Experimental observation of two regimes of expansion in localized fluidization of a granular medium

S. E. Mena,[1] F. Brunier-Coulin,[2] J. S. Curtis,[1,3] and P. Philippe[2]
[1]*Chemical Engineering, University of Florida, Gainesville, Florida 32611, USA*
[2]*IRSTEA, UR RECOVER, Aix-en-Provence, France*
[3]*College of Engineering, University of California, Davis, California 95616, USA*

(Received 11 June 2018; published 10 October 2018)

The development of localized fluidization is experimentally studied in the central plane of an immersed cohesionless granular bed using planar laser induced fluorescence and refractive index matching. The upward growth of the fluidized zone is characterized from the initial localized particle movement within a cavity to the fully fluidized state. The primary outcome of the present study is the identification of two very distinct regimes for the expansion of the fluidized cavity depending on the flow rate at the injection point: a regular regime that has been observed as in previous works, and a newly observed ultraslow regime that requires much longer time to achieve full fluidization. The ultraslow regime was formerly identified only in its nonstationary state as a cavity regime. Experimental results show that at a particular flow rate, the diameter of the injection port is a significant parameter in the evolution of the fluidization in the area close to the injection, while having almost no effect in the final phase of the expansion, provided that the granular bed is high enough. Consequently, the duration of the expansion from cavity to fluidized chimney depends strongly on the injection port size in the ultraslow regime, but only depends weakly in the regular regime. In addition, a parametric study of particle size, injection port diameter, and bed height is performed for the regular regime, based on an apparent divergence of the expansion time as the flow rate approaches a critical flow rate. For this regime, an empirical expression is developed that allows the collapse of the expansion time for all the different variables studied.

DOI: 10.1103/PhysRevE.98.042902

I. INTRODUCTION

Fluidization has been extensively studied due to its widespread application in industrial and engineering processes [1–3]. Localized fluidization refers to a special type of fluidization, where the injection of fluid is directed to a certain region of the bed, resulting in mobilization of only a portion of the particle medium. This type of fluidization is important in the operation of conical or spouted beds that are used in various operations including solids drying, biomass processing, and handling of particles with a wide size distribution [4–8]. Localized fluidization is also important in the understanding of processes like erosion and ground water movement in geology. For instance, in the context of embankment dam safety the observation of local structures commonly referred to as "sandboils" may indicate earlier stages of internal erosion [9].

Unlike traditional fluidization, there are very few experimental studies dealing with localized fluidization processes. Most of these studies focus only on the later stages of the fluidization process or the steady-state behaviors, but do not consider the initial formation stage. Moreover, studying the early behavior of localized fluidization presents experimental challenges due to the inability to observe the center of a particle bed directly. This limitation has required past studies to focus on quasi-2D geometries in shallow beds [10–17] or on geometries with injections located close to walls [18,19], where boundary interactions may become important and influence the fluidization behavior [20,21]. Conversely, other studies have been restricted to the characterization of the surface of the bed, which cannot give information on the early formation of the fluidized zone [22–24]. To directly observe the interior of a particle bed, noninvasive techniques have been successfully used, including emission particle tracking [11], magnetic resonance imaging [25,26], x-ray tomography [27], and optical visualization techniques using lasers [28,29]. The present study uses a combination of two optical techniques for direct and real-time observation of the fluidization initiation and growth: refractive index matching (RIM) and planar laser induced fluorescence (PLIF) [30]. RIM of the particles and the fluid results in a transparent medium, while PLIF allows for the observation of a selected 2D region when a fluorescent dye is added to the liquid. The fluid in contact with the planar laser reemits light at a higher wavelength, while the particles in the fluid do not fluoresce since they do not contain dye. Both refracted and reflected light can be filtered using an optical high pass filter, with the resulting image showing a 2D plane of the bed with the particles as dark regions and the fluid as clear regions. Using these techniques, the fluidization process can be observed and studied away from wall interactions, which more closely resembles the cases encountered in nature and industry.

The development of a fluidized region occurs due to the hydrodynamic interaction between the solid particle matrix and the interstitial fluid. The particles constitute a structure that is capable of sustaining a certain flow loading before being destabilized into the fluidized zone. Previous studies on granular beds subjected to localized fluid flow injection [14–16,28,29,31] showed that localized fluidization proceeds in three successive stages with increasing flow rate: an almost

static behavior except for a slight initial expansion of the bed (more noticeable at the injection location) but with no movement of particles (static regime); the formation of a region above the injection port where the particles are moving, but the top of the bed is not moving (cavity regime); and the final full fluidization, where the cavity reaches the top of the bed (chimney regime). A number of recently published numerical studies have also observed these three stages and investigated the behavior of the bed using various approaches including computational fluid dynamics, the discrete particle model, and coupled methods [11,31–35]. The purpose of the present study is to give experimental information on the transient formation and early stages of localized fluidization and to investigate the effect of different controlling parameters including the particle size, injection port diameter, and bed height. Specifically, the duration of the expansion from cavity to chimney, T_0, will be thoroughly studied. Knowledge of the development of localized fluidization and related rate of expansion is of high importance for safety of levees, dikes, and dams, especially for the cases where the development of the fluidized area is very slow.

The paper is organized as follows: A description of the experimental setup and image processing is presented in Sec. II. Section III includes the description of the experimental findings that include the classification of two regimes of expansion: a regular and an ultraslow regime. An analysis of the influence from different parameters for each regime is presented. Section IV includes a model for the critical flow rate required to achieve final full fluidization. Finally, the conclusions and final remarks are given in Sec. V.

II. EXPERIMENTAL METHODS

A. Experimental setup and optical techniques

The experimental technique and setup (Fig. 1) is the same as used in Mena *et al.* [29]; hence only a brief description will be given. Planar laser induced fluorescence (PLIF) and refractive index matching (RIM) were used to obtain videos of the early stages of fluidization in a bed of particles. As already mentioned in the introductory section, PLIF-RIM is based on the use of solid particles that have the same refractive index as the oil mixture used as medium. This combination renders a transparent system. To observe a particular plane in the bed, a fluorescent dye (red Nile, Fluka) is added to the liquid and a planar laser (Coherent, PL 532 nm 100 mW, fan angle 60°) is directed to the bed to reveal a 2D region. To counteract the natural absorption of the light from the medium and the fluid, a second laser was positioned across the particle bed directed at the same plane as the first laser. In this configuration, better quality images were possible. The reflected and refracted lights are filtered using a high-pass optical filter (Thorlabs, 580 nm) and the resulting image shows dark colored regions for the particles (no dye present) and clear regions for the liquid (dye present). The fluidization is captured either with a high-speed camera (FASTCAM SA-3 supplied by Photron, pixel resolution of 1024×1024) at 50 fps or with a standard digital camera (model MQ042MG-CM supplied by Ximea, pixel resolution of 2048×2048) at variable frame rates from 0.1 to 30 fps.

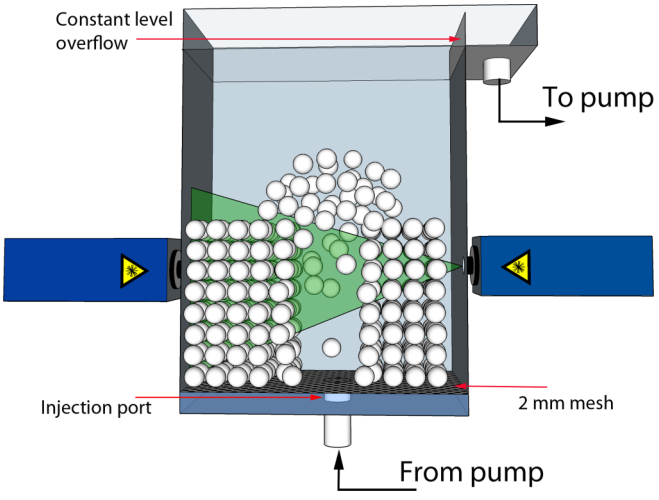

FIG. 1. Schematic of the experimental setup showing the location of the lasers. Flow from the pump is injected at the bottom of the particle bed through a variable diameter injection port. For clarity, only the plane from one laser is depicted in the figure.

The particles-medium pair was borosilicate beads in a mixture of 90% w/w mineral oil (Sigma Aldrich) and 10% w/w immersion oil type A (Cargille). The density of the borosilicate beads was 2230 kgm^{-3}. The refractive index of the glass particles was 1.472 at 23 °C as provided by the manufacturer, while the oil mixture had a refractive index of 1.472 at 23 °C as measured with an Atago refractometer. The viscosity and density of the oil mixture was 28 cP at 23 °C (measured with a cone-plate rheometer) and 845 kgm^{-3} respectively. Red Nile dye (Fluka) was added at a small concentration of approximately 5×10^{-5}% w/w.

To prepare the granular medium for the experiments, the desired injection port was installed in the bottom of a Plexiglass rectangular cell (30 cm height, 20 cm width, 10 cm depth). A constant level overflow was attached on the top of the cell to ensure a constant head. The injection port was located directly below a 2 mm mesh, which prevented the particles from falling into the upstream tube. With the injection port installed, the particles of interest were introduced into the cell to match a determined initial bed height. The oil mixture was slowly injected using a gear pump (Viking GG 4195) until complete immersion of the particles. Then, a long and smooth metallic bar was used to stir the particles to ensure a reproducible initial state and release any trapped bubbles in the bed. The solid volume fraction obtained with this protocol ϕ was 0.61 ± 0.01 for all the experiments as calculated from loading a known mass of particles into the cell and measuring the resulting height.

To conduct the experiments, the desired flow rate was programmed into the pump drive (Leroy Somer Digidrive). A calibration relation between the pump frequency and the flow rate was determined from direct sampling over the range of flow rates. The video capturing was started immediately after the pump was initialized. Video was captured until the localized fluidization was complete, as determined by the formation of the chimney. Still frames of the videos corresponding to 1, 2, 3, and 10 seconds after the onset of injection can be seen in Fig. 2. Each row corresponds to a particular

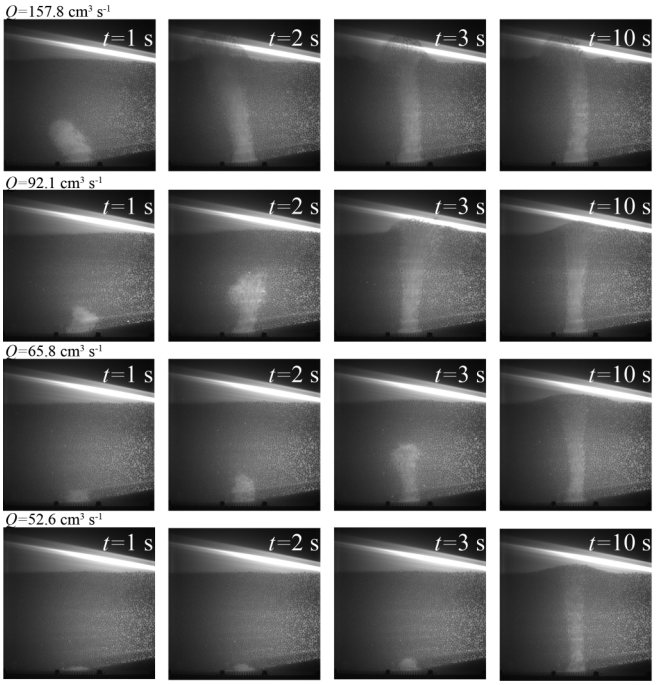

FIG. 2. Expansion of locally fluidized zone to final steady chimney fluidization for different flow rates within a bed of 3 mm particles and initial bed height of 125 mm and for an injection port of 30 mm. Sequences of transient fluidized area upward progression at successive time steps $t = 1$ s, $t = 2$ s, $t = 3$ s, and $t = 10$ s. From top to bottom the injection flow rates Q and expansion time T_0 are equal to $Q = 157.8$ cm^{3}s^{-1} and $T_0 = 1.83$ s, $Q = 92.1$ cm^{3}s^{-1} and $T_0 = 2.65$ s, $Q = 65.8$ cm^{3}s^{-1} and $T_0 = 4.15$ s, $Q = 52.6$ cm^{3}s^{-1} and $T_0 = 8.85$ s.

flow rate, with flow rate values increasing from the bottom to the top of the figure.

Particles of 3, 5, and 7 mm in diameter were tested using injection ports with diameters of 10, 20, 30, and 40 mm, at two bed heights of approximately 80 and 125 mm.

B. Image postprocessing

Video analysis was done with ImageJ by performing spatiotemporal diagrams in a vertical zone directly above the injection hole. To this end, the region of interest, or ROI [red box in Fig. 3(a) with N_z pixels height and N_x pixels width], was divided into horizontal lines with dimensions of 1 pixel height and N_x pixels width. For each horizontal line, the average intensity was calculated and plotted as a function of the z position of the horizontal line. This results in a vertical line, with dimensions of N_z pixels height and 1 pixel width. The same procedure was repeated for each consequent image in the video. Figure 3(b) shows the resulting spatiotemporal diagram, when the successive vertical lines were plotted as a function of time. From this diagram, the fluidized zone (h_f) can be observed as a brighter region due to the lower presence of particles, which are dark in the images. From Fig. 3(b), the height of the fluidized zone can be estimated at all times during the expansion resulting in Fig. 3(c). Note that a new time origin is defined at the start of liquid injection into the bed which corresponds to the beginning of the fluidized cavity expansion.

By plotting the height of the fluidized zone with respect to time, the formation of the chimney is observed. The duration of the transient regime, T_0, can be estimated from Fig. 3(c) as the time that it takes the fluidized cavity to reach the top of the bed as in (1):

$$h_f(t = T_0) = H_0, \tag{1}$$

where H_0 is the initial bed height. For instance, in Fig. 3(c) the duration of the transient regime is estimated to be 1.9 seconds. The time where this transient regime exists, or expansion time, decreases with flow rate while it diverges at lower flow rates. It is to be noted that the bed height does not change significantly during the experiments except for the region on top of the injection once the chimney is formed. The initial expansion is however limited to less than 15% of the initial bed height (H_0) as observed for instance in Fig. 3(b).

III. EXPERIMENTAL FINDINGS

A. Ultraslow and regular expansion regimes

In our previous studies [28,29] the progression of localized fluidization with increased flow rate was observed to reach three different final steady states: static bed, partially fluidized area restricted to a cavity, and full fluidized chimney. The

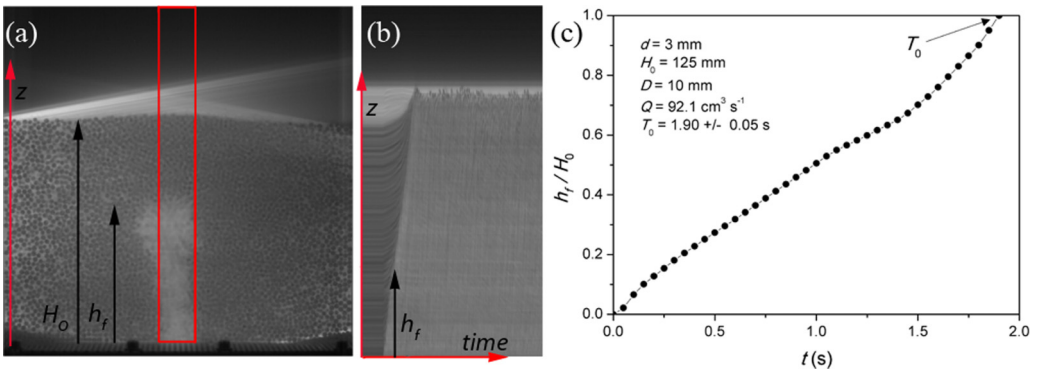

FIG. 3. (a) Rectangular box showing an example of the region where the spatiotemporal analysis is performed. (b) Spatiotemporal diagram obtained from the time evolution in the vertical stripe above the injection hole showing the height of the fluidized h_f as a brighter zone. (c) Progression of the fluidized cavity height h_f into a full chimney showing the duration of the transient process T_0.

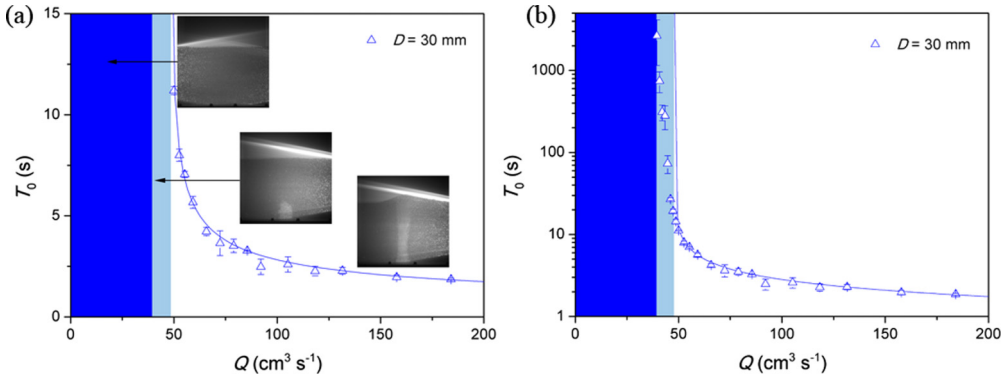

FIG. 4. Expansion time T_0 of the fluidized zone to reach a fully fluidized chimney for 3 mm particles in a bed of initial height of 125 mm and an injection port of 30 mm. Relative error bars are plotted in the figure. (a) presents the data obtained from short-time experiments and reveals, similarly to previous studies by Philippe and Badiane [28] and Mena *et al.* [29], three steady-states regimes depicted in the figure: static (dark blue region), cavity (light blue region), and chimney (white region). The curve corresponds to Eq. (3) with $\tau_0 = 2.94$ s, $Q_c = 47.94$ cm^3 s^{-1}, and $n = 0.45$ as is discussed in more detail in Sec. III B. (b) shows the additional data obtained from new experiments performed over substantially longer periods. From this graph, large but finite expansion times are observed also in the previously and mistakenly presumed steady cavity state which defines a new expansion regime called the ultraslow regime.

range of flow rates where the three steady states were observed are presented in dark blue for the static regime, light blue for the cavity regime, and white for the full chimney regime in Fig. 4. Figure 4(a) also presents a photograph of the observed state of the bed for the different behaviors. Additionally, for the chimney regime, the duration of the transient time (T_0) defined by Eq. (1) is plotted as a function of the flow rate for a bed with particles of diameter 3 mm, initial height of 125 mm, and injection diameter of 40 mm. In the vicinity of the flow rates between the cavity and chimney regime, the transient time increases sharply. This divergent relationship was described with a power law (see Eq. (4) in our previous study [28]), and allowed for the definition of a critical flow rate, Q_c, as the minimum flow rate where the transition from cavity to chimney was observed.

The data in Fig. 4(a) followed the same protocol as the previous studies [28,29] where the experiments lasted approximately 1 minute which prevented the observation of slower phenomena. To expand these findings, the current study presents further experimentations of considerably larger durations (as long as hours). The new experiments revealed that the cavity regime, which was presumed to be steady, systematically grows into a final fluidized chimney if the flow rate is maintained for a sufficiently long time, substantially higher than our previous experiments. In other words, this finding suggests that the cavity regime is an unstable state, with a very slow upward expansion. The transient time, T_0, for this new protocol with larger waiting times is plotted in Fig. 4(b) on a semilogarithmic representation for the same experimental conditions of Fig. 4(a). In light of the new data, the estimation of a consistent critical flow rate or a reliable power-law adjustment as performed for Fig. 4(a) is no longer straightforward. Note however that the critical flow rate would be substantially smaller for Fig. 4(b) compared to Fig. 4(a). Data for three other injection diameters for the same 3 mm particles and initial bed height of 125 mm are presented in Fig. 5.

From Fig. 4(b) and Fig. 5, a sharp change of kinetics is observed at lower flow rates with a considerable increase of the expansion duration time T_0. This expansion time can exceed one hour for the largest injection port of 40 mm. In the semilogarithmic representation, a change in slope is clearly noticeable around a flow rate of approximately 50 cm^{3}s^{-1} with a slight differentiation according to the injection diameter.

This insight into the evolution of the cavity allows the identification of two expansion regimes regarding not only the total duration T_0 but also the kinetics of chimney fluidization. Figure 6 illustrates the time evolution of both the normalized height of the fluidized zone, h_f/H_0, and the expansion rate, dh_f/dt, for a bed of 3 mm particles and initial height of 125 mm. The results of two flow rates are compared for the injection ports of $D = 10$ mm and $D = 40$ mm. For the sake

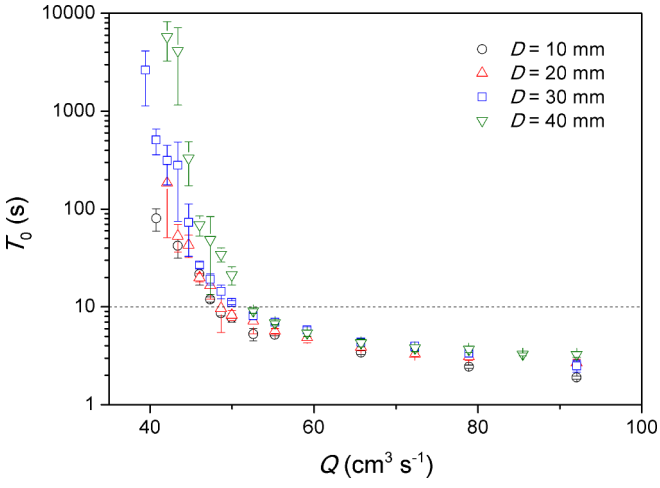

FIG. 5. Expansion time T_0 of the fluidized zone for 3 mm particles in a bed of initial height of 125 mm and for injection ports $D = 10$ mm (black circles), 20 mm (red up triangles), 30 (blue squares), and 40 mm (green down triangles). Statistical error bars are plotted in the figure. The horizontal line shows the chosen arbitrary delimitation of the ultraslow and the regular regime at $t = 10$ s as discussed in the text.

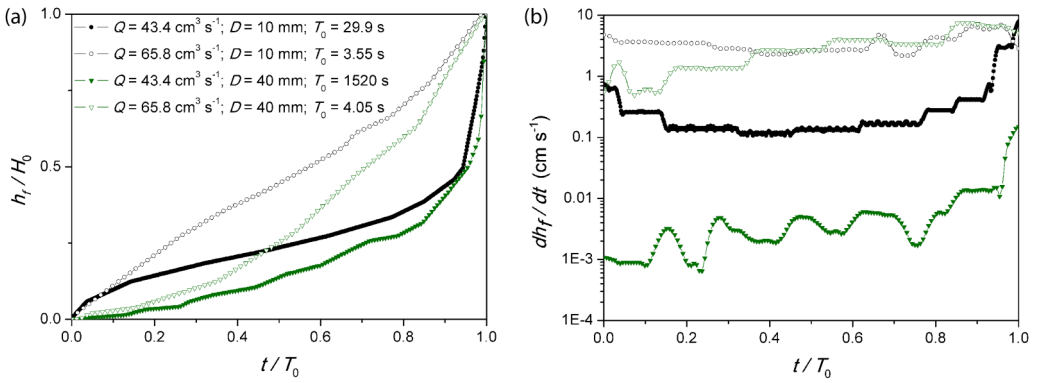

FIG. 6. Plot of (a) the normalized fluidized height h_f/H_0 and (b) the rate of expansion dh_f/dt versus the normalized time t/T_0 for $d = 3$ mm, $H_0 = 125$ mm, and $D = 10$ mm (black circles) or $D = 40$ mm (green down triangles). Typical expansions in the regular and the ultraslow regimes are observed for $Q = 65.8$ cm^3 s^{-1} (open circles) and $Q = 43.4$ cm^3 s^{-1} (closed triangles), respectively.

of clarity, the time t is also normalized by the expansion duration T_0.

Figure 6 shows the expansion of the fluidized cavity into the chimney by plotting the height of the fluidized zone h_f with time. In line with our previous findings [28], Fig. 6(a) shows an almost regular and smooth time expansion of the fluidized cavity in the regular regime for the larger flow rates (open symbols). On the contrary, a moderately lower flow rate induces an ultraslow regime with a very low expansion rate that can be up to three orders of magnitude lower during nearly all the fluidization process, except at the end when a sharp growth is observed (closed symbols). The increase of the expansion rate on a logarithmic scale is rather moderate in the regular regime (open symbols) compared to what is observed in the ultraslow regime (closed symbols).

Moreover, it can be noted from Fig. 5 that there is a strong dependency of T_0 on the injection diameter in the ultraslow regime (smaller flow rates), while the latter remains weak and almost negligible in the regular regime (higher flow rates). The influence of the injection diameter is also observed in the kinetics of fluidization in Fig. 6(b) since, for the same flow rate $Q = 43.4$ cm^3 s^{-1}, the rate of expansion is almost two orders of magnitude lower for $D = 40$ mm compared to $D = 10$ mm.

An additional distinction between the two regimes can be observed in Fig. 7 where the standard deviation of the expansion time is plotted for different flow rates. For these series of experiments the standard deviation, ΔT_0, was calculated from three to five different trials and normalized by the average value T_0 for a bed with $d = 3$ mm, $H_0 = 125$ mm, and $D = 10, 20, 30$, and 40 mm. The ultraslow regime ($Q < 50$ cm^3 s^{-1}) has an almost systematically and significantly higher standard deviation than the regular expansion regime ($Q > 50$ cm^3 s^{-1}). However, comparing the data for the different injection sizes D, it is difficult to find an obvious delimitation between the two regimes and more statistics would probably be needed. Nonetheless, based more specifically on the data in Fig. 5 but in reasonable agreement with Fig. 7, the frontier between the ultraslow and regular expansion for the 3 mm particles in a bed with initial height of 125 mm is defined as $T_0 = 10$ s [as anticipated in Fig. 4(a)].

A last point regarding the steady states concerns the static regime. Indeed, as the kinetics of the ultraslow regime can become drastically slow, it is not possible to propose a clear delimitation between static and cavity state. Presumably, if even a very slight cavity appears when fluid injection is switched on, it is likely that the system will ultimately reach a chimney-like fully fluidized state. However, further investigation needed to validate this hypothesis would require inordinately long experiments.

The following sections propose a comparison of the regular and ultraslow expansion regimes in terms of kinetics and duration, with a specific focus on the influence of the injection port diameter (Sec. III B). A systematic analysis of the regular regime follows, with the proposal of an empirical scaling for the expansion time that accounts for all the different influences: particle diameter and density, fluid properties, injection diameter, and bed height (Sec. III C).

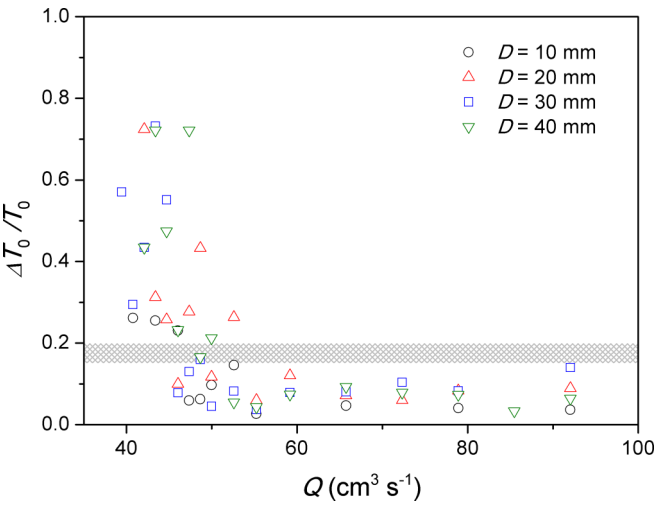

FIG. 7. Relative standard deviation of the expansion time T_0 for different flow rates and for $d = 3$ mm, $H_0 = 125$ mm, and $D = 10, 20, 30$, and 40 mm with same symbol convention as in Fig. 5. The standard deviation was calculated from three to five different experiments. The hatched area is an arbitrary delimitation between $\Delta T_0/T_0 = 0.15$ and 0.20 that approximately separates higher values of relative standard deviations. The frontier is almost consistent with the one between ultraslow and regular regimes proposed in Fig. 5.

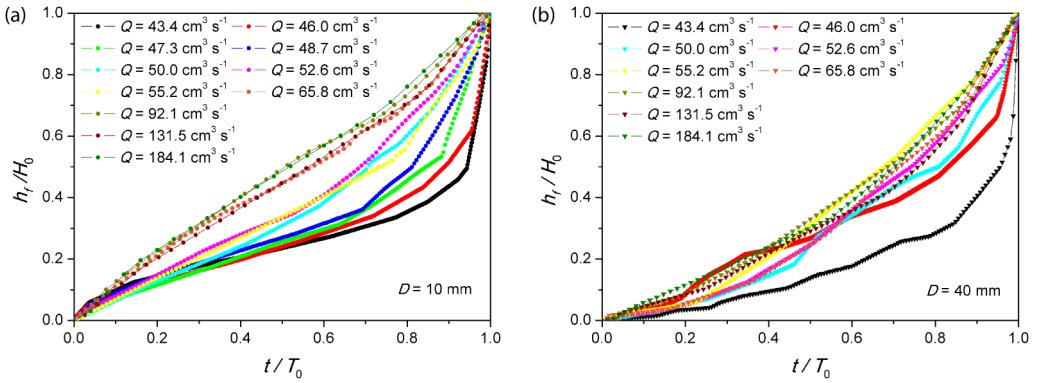

FIG. 8. Plot of h_f/H_0 versus t/T_0 at different flow rates for 3 mm particle bed with initial bed height of 125 mm and injection port of (a) $D = 10$ mm and (b) $D = 40$ mm.

B. Kinetics of the expansion

The ultraslow regime was studied for the 3 mm particles in a bed of height 125 mm for the 4 different injection port diameters $D = 10$, 20, 30, and 40 mm. Each experiment lasted a considerable amount of time and required replicates to perform the statistical analysis, which prevented the study of other bed heights and particle diameters. Although conclusions are limited to the impact of the injection port diameter on the expansion time T_0, these experiments suffice to analyze how the kinetics of expansion changes from the ultraslow to the regular regime.

A simple assumption would be to hypothesize that the kinetics of the expansion is controlled only by the total expansion duration T_0. To test this hypothesis, a plot of h_f/H_0 versus t/T_0 is shown in Fig. 8 for $D = 10$ mm and $D = 40$ mm. As soon as the flow rate exceeds roughly 55–60 $\mathrm{cm^3 s^{-1}}$, all the curves present a fair collapse. This typical flow rate is almost consistent, although slightly larger than the approximate value of 50 $\mathrm{cm^3 s^{-1}}$ corresponding to the proposed delimitation $T_0 = 10$ s between the ultraslow and regular regimes.

In addition, the shapes of the expansion curves are slightly different in both the ultraslow and the regular regimes for the injection of $D = 10$ mm: In the ultraslow regime, a concave portion is observed during the first stage of the expansion before turning to a terminal convex shape. On the contrary, for $D = 40$ mm the form of the expansion curve remains always convex for both the ultraslow and the regular regime. In addition, at the latter stages of the expansion (larger t/T_0), it can be noted that for both injection diameters the shape of the curves is very similar, suggesting that the influence of the injection size is less noticeable as the cavity grows.

From this observation, it can be concluded that the regular regime presents a unique kinetics of expansion for each injection diameter, which can be approximately parametrized by the local expansion duration T_0. Moreover, keeping only the data well inside the regular expansion regime ($Q > 60$ $\mathrm{cm^3\ s^{-1}}$), a plot of $\ln(h_f/H_0)$ vs $(T_0 - t)/T_0$ suggests a linear relation when t approaches T_0, as shown in Fig. 9. This means that after an initial phase, the height of the cavity h_f grows exponentially with time, $h_f \propto \exp(\sigma t)$, as expected from linear stability theory (see for instance [36]), where the instability growth rate σ is inversely proportional to the expansion time T_0. Note that the influence of the injection diameter remains in the value of the proportionality coefficient: ~1.6 for $D = 10$ mm against ~2.5 for $D = 40$ mm. Note also that here again a better collapse, within a larger time range, is found for $D = 10$ mm compared to $D = 40$ mm.

As mentioned in Fig. 5, an increase in the injection diameter D considerably slows down the upward expansion of the fluidized region in the ultraslow regime. This trend is in contrast with the regular regime where the injection port diameter was found to have a rather limited effect as will be discussed in the next section dealing with the regular regime. The larger expansion times observed for larger injection port diameters can be explained by the difference in fluid velocity; for the same flow rate, the velocity developed in a 40 mm injection port is substantially smaller than the one developed in a 10 mm one. The slower velocities probably lead to longer kinetics of expansion in the vicinity of the injection hole. Recent numerical results using 2D DEM-LBM modeling [31]

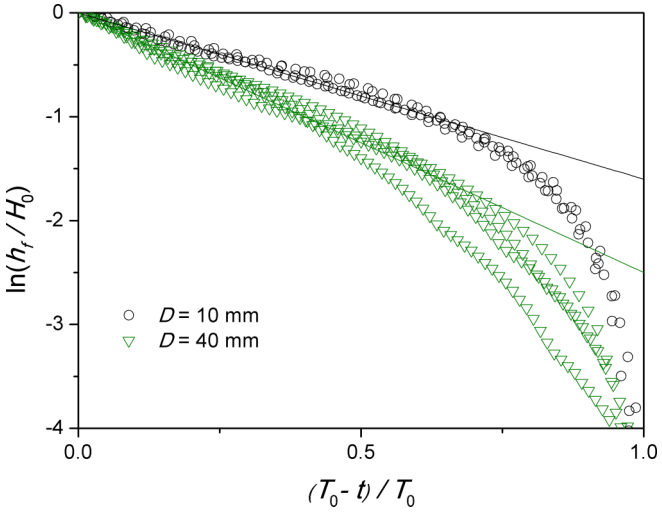

FIG. 9. Plot of natural logarithm of the dimensionless height of the cavity h_f/H_0 vs the dimensionless time $(T_0 - t)/T_0$ in the regular regime. Data from Fig. 8(a) with $D = 10$ mm (black open circles) and Fig. 8(b) with $D = 40$ mm (green open down triangles) restricted to $Q > 60$ $\mathrm{cm^3\ s^{-1}}$. The solid lines stand for approximate linear relation with slope equal to -1.6 and -2.5 for $D = 10$ mm and $D = 40$ mm, respectively.

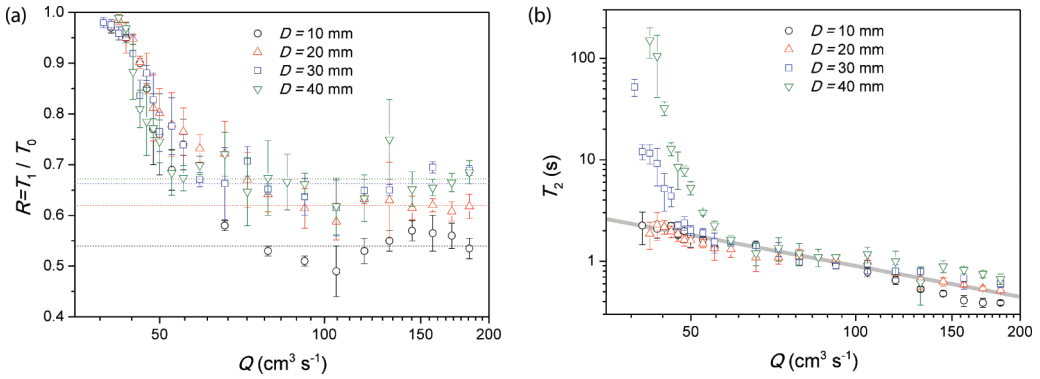

FIG. 10. Semilogarithmic plot of (a) the ratio $R = T_1/T_0$ where the horizontal lines stand for the constant value R_∞ reached in the regular regime and (b) the terminal expansion timescale T_2 for $d = 3$ mm, $H_0 = 125$ mm, and $D = 10, 20, 30$, and 40 mm. The solid line in gray stands for an empirical expression $T_2 \propto Q^{-1}$ with a coefficient equal to 90 cm^3.

show that as the fluidized zone expands, the cross section progressively enlarges if the injection port is small and inversely reduces if the injection port is large. As a result, the cavity progressively tends to a similar dimension when approaching the top of the bed and consequently becomes less dependent on the injection diameter. This means that the initial expansion is highly sensitive to the injection diameter, with a local fluid velocity that can be four times smaller comparing $D = 40$ mm and $D = 10$ mm, and could explain why T_0 varies by over 1 order of magnitude. On the contrary, the last part of the expansion is almost independent of the injection diameter since the chimney reaches a similar diameter regardless of the injection port used.

One additional point to make regarding the independence of the injection port in the latter stages of the expansion concerns the initial bed height. The change in diameter of the cavity requires a certain distance in the bed to develop and reach an equilibrium width, independent of the initial injection diameter. For this reason, it is hypothesized that a minimum initial bed height is required to observe the independence of the final expansion rate on injection port diameter. In beds with initial heights that are too small to allow significant expansion or contraction of the chimney as the cavity grows, the influence of the injection diameter on the final expansion of the fluidized cavity will remain visible.

On the basis of these findings, it could be assumed that the expansion of the fluidized zone can be divided into two parts with two distinct and separate kinetics: first, an initial expansion in direct vicinity of the injection port and highly controlled by the injection diameter; second, a final expansion that tends to be invariant regardless to the injection geometry as long as the granular bed is high enough. Based on these ideas, it is consistent to suggest the duration of the initial expansion becomes increasingly predominant in the ultraslow regime compared to the time needed for the final expansion, while both times remain in the same order of magnitude in the regular regime.

To further test this explanation, the bed was arbitrarily divided into two equal parts in order to measure the time T_1 needed for the expanding fluidized cavity to reach half the bed height, $h_f(t = T_1) = H_0/2$. Then the time T_2 needed to complete the full chimney fluidization up to H_0 is simply given by $T_2 = T_0 - T_1$.

The ratio $R = T_1/T_0$ is plotted in Fig. 10(a) as a function of the flow rate. As can be seen, R tends to 1 when the flow rate decreases, meaning that T_1 indeed becomes more predominant in the ultraslow regime compared to T_2. There is only a weak dependence of the injection port on R in the ultraslow regime. Inversely, in the regular regime, R quickly stabilizes to a constant value R_∞ that depends on the injection diameter D: $R_\infty = 0.540 \pm 0.030, 0.619 \pm 0.016, 0.663 \pm 0.028$, and 0.672 ± 0.033 for $D = 10, 20, 30$, and 40 mm, respectively. The error was estimated from the standard deviation of repeated experiments. By way of comparison, note that a value of R_∞ equal to 0.5 would be found for an expansion linear with time and $\sqrt{2}/2 \approx 0.707$ for a quadratic evolution.

Then, the duration T_2 of the second half of the expansion versus flow rate is shown in Fig. 10(b). On this graph, it is remarkable that for both data obtained with $D = 10$ mm and $D = 20$ mm, there is no change in the slope between regular and ultraslow regimes. Additional comments concern (i) the occurrence of slight sensitivity on injection diameter D at large flow rates, and (ii) the empirical proposal of a general trend for T_2 as $T_2 \propto Q^{-1}$. Note that for the larger flow rates, a weak although clear differentiation is observed with D, the kinetics being faster for a smaller injection diameter, that is to say, for a higher injection velocity.

The use of T_2 as a more pertinent characteristic time suggests that in general, the terminal phase of the expansion tends to kinetics with a unique timescale given by flow rate, at least for small enough injection diameter. Plotting h_f/H_0 versus $(T_0 - t)/T_2$ for the same data from Fig. 8(a), Fig. 11(a) shows a collapse in the range $h_f > H_0/2$ for all flow rates. The generic law for the final expansion is compatible with an exponential as already noticed from Fig. 9 and can consequently be written as follows:

$$\frac{h_f}{H_0}(t) = \exp\left[-\ln(2)\left(\frac{T_0 - t}{T_2}\right)\right] \quad \text{for} \quad 0 < T_0 - t < T_2. \tag{2}$$

However, Fig. 11(b) shows that if a similar treatment is given to the data for $D = 40$ mm in Fig. 8(b), the collapse is significantly less conclusive. In fact, even if h_f/H_0 is taken as 3/4 instead of 1/2 for the definition of T_1 and T_2, the

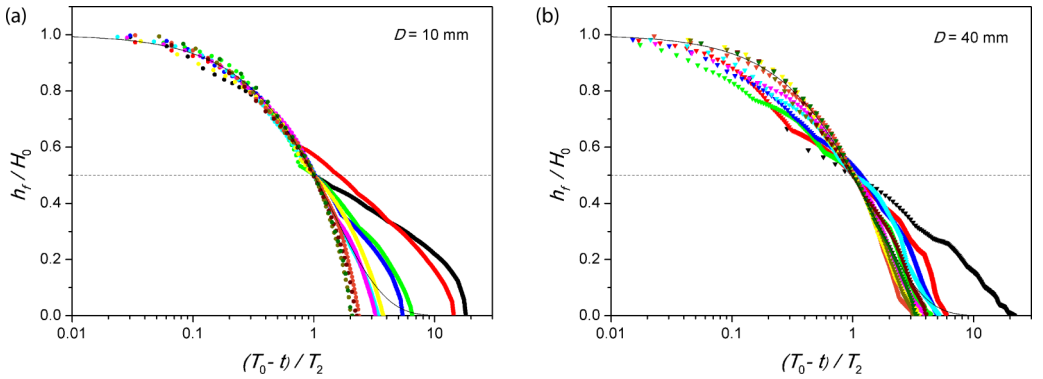

FIG. 11. Semilogarithmic plot of h_f/H_0 versus $(T_0 - t)/T_2$ for (a) $D = 10$ mm and (b) $D = 40$ mm for the same data and same symbol convention as presented in Fig. 8. The solid line stands for the terminal expansion law given in Eq. (2) while the dashed line indicates the delimitation $h_f/H_0 = 1/2$ used to define T_1 and T_2.

collapse is only marginally improved (data not shown). This means that the final expansion is still influenced by a large enough injection diameter. Most probably this influence must be reduced as the bed height increases and it can be reasonably speculated that for thicker beds the generic terminal expansion [Eq. (2)] should be recovered. Further experiments would be needed to validate this hypothesis.

Compared to the collapse in Fig. 9 where h_f/H_0 was plotted against $(T_0 - t)/T_0$, Eq. (2) allows for a general relationship, independently of injection diameter D. The slopes obtained in Fig. 9 are compatible with this finding: recalling that $T_1 = R_\infty T_0$, the slope in Fig. 9 is given by $-\ln 2/(1 - R_\infty)$ resulting in -1.5 ± 0.1 for $D = 10$ mm and -2.1 for $D = 40$ mm, which is roughly comparable to -1.6 and -2.5 extracted from Fig. 9.

In summary, these experiments show that there is a great influence of the injection port diameter on the kinetics of the expansion of the fluidized zone in the ultraslow regime. The influence is due to the initial stages of the expansion where the smaller injection ports induce higher fluid velocities and result in a faster growth of the cavity height h_f. In the latter stages, the influence of the injection port tends to vanish, provided that the bed height is sufficiently large. An investigation of the regular expansion regime follows, where a parametric study will be presented to determine the influence of the injection port size, the diameter of the particle, and the initial bed height.

C. Parametric study of the regular regime

The duration of the transient fluidization, T_0, for the regular regime (i.e., for $T_0 < 10$ s) is presented in Fig. 12. As mentioned before, T_0 decreases with increasing flow rate following a power-law function and apparently diverges when approaching the critical flow rate Q_c . This behavior is in agreement with previous results [28] and follows the relation

$$T_0 = \tau_0 \left(\frac{Q}{Q_c} - 1 \right)^{-n}, \tag{3}$$

where τ_0 is the transient time T_0 obtained for $Q = 2Q_c$ and where the exponent value, determined using a nonlinear regression, remains in the range of $0.3 < n < 1.1$ (see forthcoming Fig. 16). The critical flow rate Q_c together with the exponent n and the characteristic time τ_0 are determined from the power-law adjustment.

The average expansion rate of the fluidized zone can be described as $V_0 = \frac{H_0}{T_0}$. Consequently, the mean expansion rate V_0 obeys the power-law relation

$$V_0 \propto (Q/Q_c - 1)^n. \tag{4}$$

Equation (4) is plotted in Fig. 13 for the 3, 5, and 7 mm particles for different bed heights and injection ports. As observed from the different slopes for the four cases presented, the proportionality coefficient is not constant and can be a function of the particle diameter d, the injection port diameter D, and the initial bed height H_0. All these potential dependencies will be successively tested.

First, the influence of the injection port D can be tested by plotting the expansion rate versus $(Q/Q_c - 1)^n$ for the same bed height and particle diameter for different injection diameters as in Fig. 14 for a bed of initial height of 125 mm and

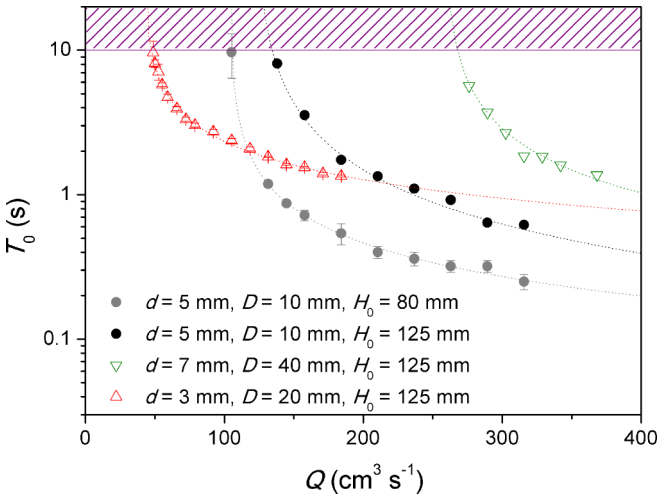

FIG. 12. Typical evolutions of the duration of the transient regime versus flow rate showing the decrease in the expansion time with increase in flow rate for different sets of control parameters. All curves diverge when approaching a critical flow rate according to Eq. (3) (in dotted lines). The hatched area shows the region for the ultraslow regime ($T_0 > 10$ s).

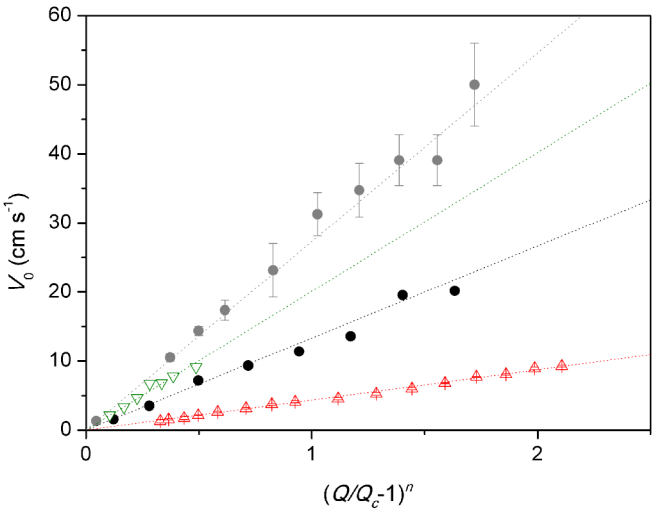

FIG. 13. Typical evolution of the mean expansion rate V_0 versus $(Q/Q_c - 1)^n$ for the same data as in Fig. 12 using the same nomenclature. The values for n are the ones found in the nonlinear regression analysis in Fig. 12.

particles with diameters of 3, 5, and 7 mm. It can be concluded from Fig. 14 that there is roughly no distinguishable influence of the injection diameter D.

Contrary to the lack of relation observed between the expansion rate and the size of the injection port, a dependency with particle diameter d is clearly observed in Fig. 14. As shown in the lines, there is a proportionality relation between V_0 and $(Q/Q_c - 1)^n$ with a coefficient c that increases from $c = 4.8 \pm 0.1$ cm s^{-1} for $d = 3$ mm, to $c = 11.3 \pm 0.3$ cm s^{-1} for $d = 5$ mm, and finally $c = 18.6 \pm 0.4$ cm s^{-1}

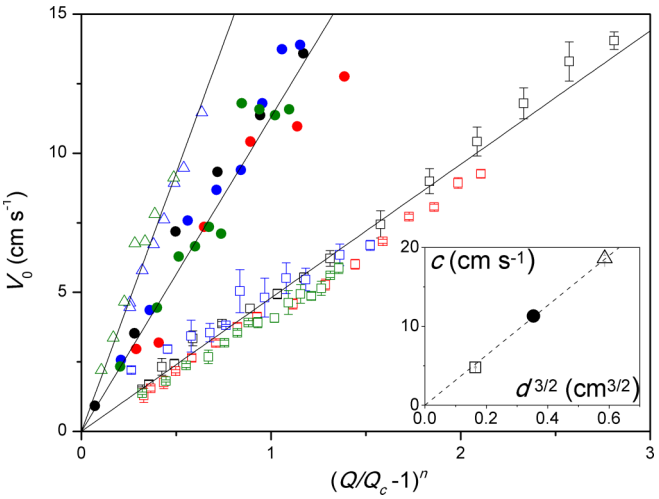

FIG. 14. Mean expansion rate V_0 versus $(Q/Q_c - 1)^n$ for a bed of initial height $H_0 = 125$ mm for the different injection sizes $D =$ 10 mm (black), 20 mm (red), 30 mm (blue), 40 mm (green), and particle diameters $d = 3$ mm (square), 5 mm (circle), and 7 mm (triangle). The solid lines represent proportionality law with coefficient c of 4.8, 11.3, and 18.6 cm s^{-1}, respectively. Inset: Plot of the proportionality coefficient c between V_0 and $(Q/Q_c - 1)^n$ versus $d^{3/2}$. The dashed line stands for the power-law relation $c = ad^{3/2}$ with $a \sim 31.6$ cm$^{-1/2}$ s^{-1}.

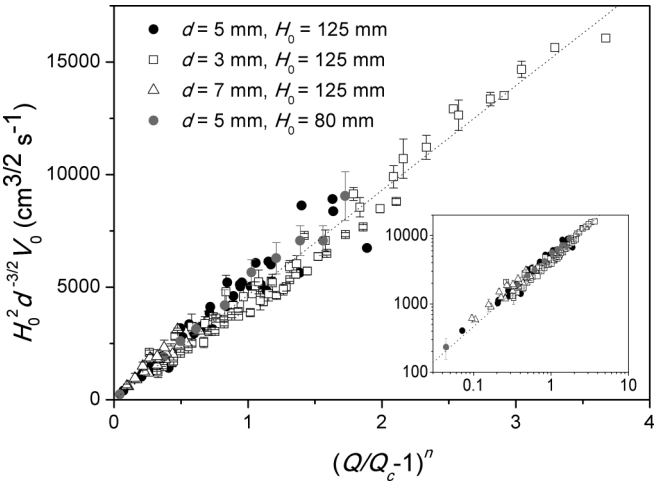

FIG. 15. Plot of $H_0^2 d^{-3/2} V_0$ versus $(Q/Q_c - 1)^n$ for all the data. The dotted line stands for a proportionality relation with a coefficient $B \sim 4650$ cm$^{3/2}$ s^{-1}. Inset: Same data in log-log representation.

for $d = 7$ mm. This influence of the particle diameter on c is perfectly compatible with a power-law relation: $c \propto d^{3/2}$ as shown in the inset of Fig. 14.

Finally, as can be noticed in Fig. 12 comparing the data obtained for same injection diameter and particle diameter but different bed height, there is still a remaining dependency of the mean expansion V_0 with the initial bed height H_0. This dependency could be empirically accounted for by $V_0 \propto H_0^{-2}$ which, together with the dependency on particle diameter, allows for an approximate collapse of all the data as shown in Fig. 15:

$$V_0 \propto H_0^{-2} d^{3/2} \left(\frac{Q}{Q_c} - 1 \right)^n . \tag{5}$$

Note that H_0 impacts also the critical flow rate Q_c as discussed in more details in forthcoming Sec. IV.

From this analysis, the injection diameter D has a very negligible influence on the transient regime. But Fig. 16 suggests otherwise where a dependency with D is observed for the exponent n of the power law. The exponent n decreases, almost linearly, with the ratio D/d. Although the data scattering is probably too high to reach a definitive conclusion, the relation in Eq. (6) can be proposed as an empirical relation:

$$n = 1 - \frac{D}{18d}. \tag{6}$$

IV. CRITICAL FLOW RATE FOR CHIMNEY FLUIDIZATION FROM TRANSIENT EXPERIMENTS

This section introduces a model to predict the critical flow rate, defined as the flow rate required to achieve a chimney behavior. The model is derived from the divergent power-law fit from the transient experiments in the regular expansion regime.

The model, presented in more detail in [29], assumes that the nonhomogeneous fluidization of the bed changes in the upper part of the bed to a simple homogeneous fluidization

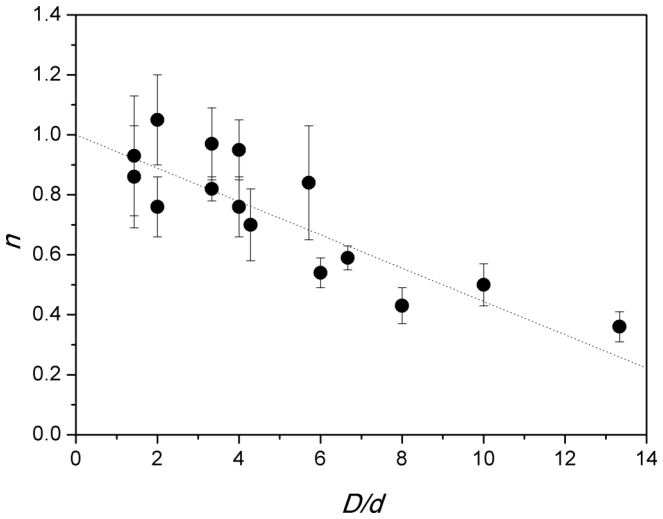

FIG. 16. Plot of the exponent n versus the ratio D/d for all the data. The dotted line stands for the linear relation $n = 1 - \frac{D}{18d}$.

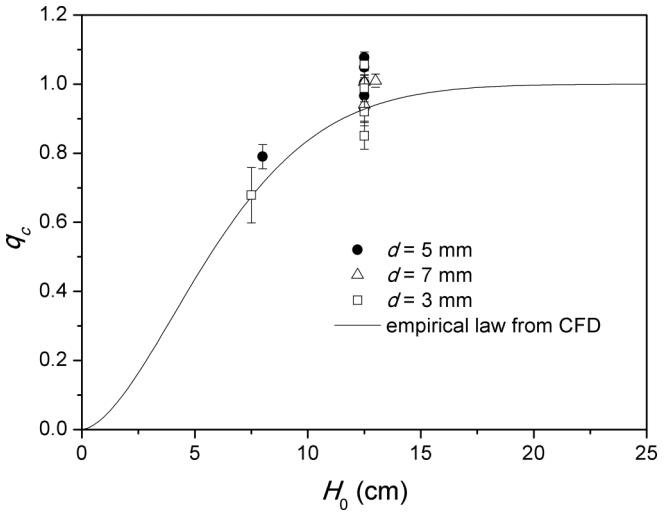

FIG. 17. Plot of q_c versus H_0 for all the data. The solid line stands for the empirical relation of $f(H_0)$ deduced from CFD calculation detailed in [29].

within a chimney of cross section S_{ch}, whose value is *a priori* unknown. This hypothesis requires that, in the upper exit of the chimney, the critical velocity U_c^h of homogeneous fluidization within a monodisperse particulate bed is reached. The critical velocity U_c^h is

$$U_c^h = \frac{(1-\phi)^3}{10\phi}\frac{\Delta\rho g d^2}{18\eta} = \beta d^2, \tag{7}$$

where ϕ is the solid volume fraction prior fluidization of the bed, $\Delta\rho$ is the difference between the density of the solid and liquid, and η is the viscosity. A convenient way to test this model suggests introducing a reduced critical flow rate q_c as

$$q_c = \frac{Q_c}{S_b U_c^h}. \tag{8}$$

This quantity compares the mean velocity that would have been obtained for a uniform injection, namely Q_c/S_b (with S_b the whole bed's cross section), to the critical velocity for homogeneous fluidization. It should logically increase with injection diameter D and progressively saturate to 1 as approaching uniform injection condition when D tends to the size of the experimental cell.

A plot for the reduced critical flow rate q_c with respect to the initial bed height H_0 is shown in Fig. 17 and confirms this general trend. A quantitative comparison with the model can be obtained from computational fluid dynamics (CFD) calculations. The latter were conducted in Fluent (Ansys) and the details can be found in our previous work [29]. In brief, simulations of a 3D porous bed with identical geometry to the one used in the experiments were conducted. The permeability of the bed was fixed by the Carman-Kozeny expression [37] for each of the three different particle diameters. The velocity developed in the bed was obtained for different conditions of injection port and bed height. Then, the reduced critical flow rate was calculated using

$$q_c^{\mathrm{CFD}}(H_0, \mathrm{S}_{ch}, D,\ d) = \frac{\frac{1}{S_b}\iint_{S_b} u dS}{\frac{1}{S_{ch}}\iint_{S_{ch}} u dS}, \tag{9}$$

where u is the vertical component of the fluid velocity at the top surface of the bed and S_b and S_{ch} are the cross section of the bed and the fluidized chimney, respectively.

As stated previously [29], dependencies on S_{ch}, D, and d were found to be weak, and almost negligible, resulting in the following empirical relation:

$$q_c^{\mathrm{CFD}}(H_0) = 1 - \exp\left[-\left(\frac{H_0}{H_0^*}\right)^{\alpha}\right], \tag{10}$$

where $\alpha \approx 5/3$ and $H_0^* \approx 70$ mm. H_0^* is an empirical parameter that physically corresponds to the distance needed for a locally injected flow to homogenize in a porous medium.

This empirical relation is plotted in Fig. 17, where an approximate agreement is observed but with some scattering and a global overestimation. As discussed hereafter, this is due to a slight influence of injection diameter and to some uncertainty in the viscosity and solid volume fraction estimates for the calculation of U_c^h.

Indeed, to improve the agreement between the data and the model, U_c^h can be used as free parameter for each particle diameter. This was done for the data obtained at $H_0 = 125$ mm for $d = 3$ mm, $d = 5$ mm, and $d = 7$ mm. Practically speaking, for each particle diameter d, U_c^h is manually adjusted to get a collapse of the data and to center it along the CFD prediction $f(H_0 = 125\ \mathrm{mm}) \approx 0.928$. This new adjusted value of the critical velocity allows for the calculation of an adjusted value, q_c^a, of the reduced critical flow rate. As shown in Fig. 18, these adjusted values of the reduced critical flow rate q_c^a show a better agreement with the model, for the averaged value from the data obtained with height $H_0 = 125$ mm that have been used to adjust U_c^h, but also for the results with $H_0 = 75$ and 80 mm. The inset shows the values obtained for U_c^h as a function of diameter d. As expected from the theory, these values of U_c^h are compatible with a quadratic dependence on particle diameter d. The proportionality coefficient is $\beta_{\mathrm{exp}} \approx 2.69\ \mathrm{cm}^{-1}\ \mathrm{s}^{-1}$, which is in good agreement with the theoretical prediction $\beta_{\mathrm{th}} = 2.62 \pm 0.43\ \mathrm{cm}^{-1}\ \mathrm{s}^{-1}$, calculated from Eq. (7) accounting for experimental uncertainties on

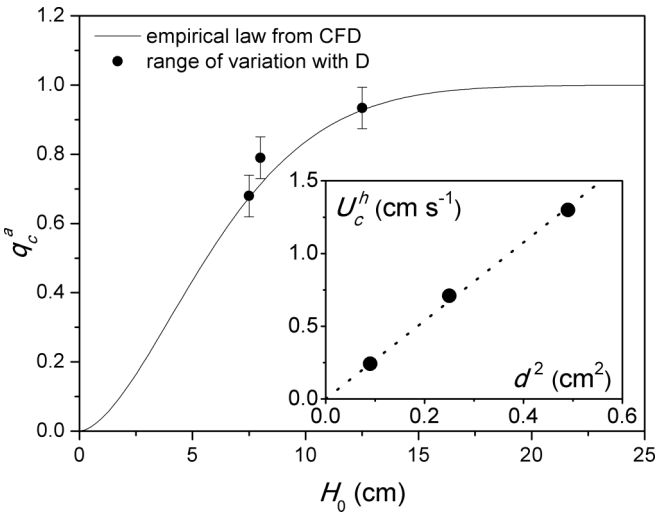

FIG. 18. Adjusted values of q_c versus H_0 obtained from the data in Fig. 17. The solid line stands for the empirical relation of $f(H_0)$ deduced from CFD calculation and the error bars show the range of variation due to the injection diameter D. Inset: Values of U_c^h after manual adjustment as a function of particle diameter d. The dashed line stands for the quadratic relation $U_c^h = \beta d^2$ [see Eq. (7)] with a proportionality coefficient $\beta_{\text{exp}} = 2.69\ \text{cm}^{-1}\ \text{s}^{-1}$.

solid volume fraction ($\phi = 0.61 \pm 0.01$) and viscosity ($\eta = 0.28 \pm 0.02$ g cm^{-1} s^{-1}).

Regarding the injection diameter influence, Fig. 19 shows that for $H_0 = 125$ mm with $d = 3$ mm, $d = 5$ mm, and $d = 7$ mm, q_c^a is slightly but continuously increasing with injection diameter reaching almost a 15% increase for $D = 40$ mm compared to $D = 10$ mm. Note that this second-order effect of the injection diameter was observed to be almost negligible although present in the CFD calculations.

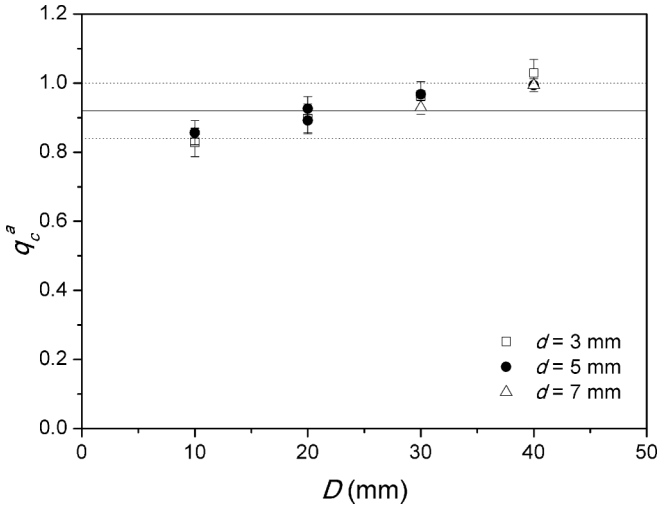

FIG. 19. Adjusted values of the reduced critical flow rate q_c^a versus D for $H_0 = 125$ mm and bead diameters $d = 3$, 5, and 7 mm. The solid line stands for the value expected from the CFD calculation while the dotted lines show approximately the range of variation due to the influence of the injection diameter.

Although a linear dependency is roughly observed in Fig. 19, the trend is not realistic for larger injection ports as the condition $q_c = 1$ must be met for a homogeneous fluidization configuration, in other words, when D approaches the dimensions of the experimental cell.

V. CONCLUSIONS

The formation and growth of localized fluidization in a particle medium is studied. Two regimes of expansion are found: a regular expansion regime, where the cavity tends to grow in an exponential way until it reaches fully localized fluidization; and an ultraslow regime at moderately smaller flow rates, where the cavity grows very slowly in the early stages and presents a faster expansion in later stages. More precisely, the ultraslow regime can be distinguished from the regular regime by (1) a longer transient time between the formation of the cavity and the development of a full chimney, (2) a very small change in the fluidized cavity height in the initial stages with a fast expansion at later stages, (3) an expansion rate that is significantly dependent on the injection port size, and (4) a higher standard deviation in the expansion time, resulting in a less repeatable process. The kinetics of the expansion is also dependent on the regime, with the regular regime having an almost continuous rate of expansion through time and the ultraslow presenting a variable expansion. In fact, two stages of the expansion are found in the ultraslow regime, with an initial expansion controlled by the injection diameter, and a secondary expansion that tends to be independent of the injection port at the terminal stages under the condition that the bed's height is large enough.

A question arises as to whether all cavities will grow into a chimney at any flow rate given enough time. For the present experiments, the behavior of the bed was observed for a maximum of two hours, so it is possible that some flow rates could reach a full fluidization stage after longer injection times. However, it is worth noting that in all cases where the full chimney was observed, an initial void expansion close to the injection port was formed at the start of the fluid flow. Consequently, it is speculated that a fluidized chimney may be ultimately reached if a localized bed's dilation can be induced by the fluid flow at injection. Below this threshold the bed is assumed to behave as a simple porous medium.

The injection port diameter is found to have a marked effect in the kinetics of expansion of the ultraslow regime, whereas it only has a secondary effect in the regular regime. The fairly different fluid velocities developed close to the injection port for the same flow rate can explain the different behaviors.

A parametric study was carried out for the regular regime to test the dependencies of the particle size, injection port diameter, and initial bed height on the duration of the expansion. The diameter of the particle and the bed height have the most significant effect on the behavior of the cavity, with the diameter of the injection port having a lesser effect. A model based on a power-law equation is developed to account for each of the dependencies and resulted in a collapse of the data.

Finally, a model to determine the critical flow rate needed to achieve fluidization in the regular regime is presented. The model uses the critical velocity to achieve homogeneous

fluidization as a free parameter. The results of the model are in agreement with a previous CFD simulation carried out in a bed with the same characteristics of the experimental setup.

ACKNOWLEDGMENT

Funding from NSF OISE 0968313 is gratefully acknowledged.

[1] M. Kwauk, *Fluidization* (Science Press, Beijing, 1992).
[2] M. Rhodes, *Introduction to Particle Technology* (Wiley, Chichester, 2004).
[3] D. Kunii and O. Levenspiel, *Fluidization Engineering* (Butterworth-Heinemann, Boston, 1991).
[4] M. Wormsbecker, T. Pugsley, and H. Tanfara, Chem. Eng. Sci. **64**, 1739 (2009).
[5] R. Aguado, M. Olazar, M. J. San José, G. Aguirre, and J. Bilbao, Ind. Eng. Chem. Res. **39**, 1925 (2000).
[6] A. R. Fernandez-Akarregi, J. Makibar, G. Lopez, M. Amutio, and M. Olazar, Fuel Process. Technol. **112**, 48 (2013).
[7] W. Permchart and V. I. Kouprianov, Bioresource Technol. **92**, 83 (2004).
[8] H. Tanfara, T. Pugsley, and C. Winters, Drying Technol. **20**, 1273 (2002).
[9] *Erosion in Geomechanics Applied to Dams and Levees*, edited by S. Bonelli (John Wiley & Sons, New York, 2013).
[10] R. J. Nichols, R. S. J. Sparks, and C. J. N. Wilson, Sedimentology **41**, 233 (1994).
[11] M. S. van Buijtenen, W. van Dijk, N. G. Deen, J. A. M. Kuipers, T. Leadbeater, and D. J. Parker, Chem. Eng. Sci. **66**, 2368 (2011).
[12] N. Almohammed, F. Alobaid, M. Breuer, and B. Epple, Powder Technol. **264**, 343 (2014).
[13] Falah Alobaid and Bernd Epple, Particuology **11**, 514 (2013).
[14] P. Rigord, A. Guarino, V. Vidal, and J. Géminard, Granular Matter **7**, 191 (2005).
[15] G. S. S. R. K. Sastry, G. S. Gupta, and A. K. Lahiri, ISIJ Int. **43**, 153 (2003).
[16] M. A. Thaha, R. Triatmadja, and A. I. Dwipuspita, Int. J. Hydraul. Eng. **2**, 85 (2013).
[17] A. Nermoen, C. Raufaste, S. D. deVilliers, E. Jettestuen, P. Meakin, and D. K. Dysthe, Phys. Rev. E **81**, 061305 (2010).
[18] Y. He, D. Z. Zhu, T. Zhang, Y. Shao, and T. Yu, J. Hydraul. Eng. **143**, 6017007 (2017).
[19] M. O. A. Alsaydalani and C. R. I. Clayton, J. Geotech. Geoenviron. Eng. **140**, 4013024 (2014).
[20] V. Zivkovic, M. J. Biggs, and Z. T. Alwahabi, AIChE J. **59**, 361 (2013).
[21] M. Aghajani, H. Müller-Steinhagen, and M. Jamialahmadi, Dev. Chem. Eng. Miner. Process. **12**, 403 (2004).
[22] F. Zoueshtiagh and A. Merlen, Phys. Rev. E **75**, 056313 (2007).
[23] T. Mörz, E. A. Karlik, S. Kreiter, and A. Kopf, Sediment. Geol. **196**, 251 (2007).
[24] J. A. Ross, J. Peakall, and G. M. Keevil, Sedimentology **58**, 1693 (2011).
[25] M. H. Khöl, G. Lu, J. R. Third, K. P. Prüssmann, and C. R. Müller, Chem. Eng. Sci. **109**, 276 (2014).
[26] M. H. Köhl, G. Lu, J. R. Third, M. Häberlin, L. Kasper, K. P. Prüssmann, and C. R. Müller, Chem. Eng. Sci. **97**, 406 (2013).
[27] G. T. Seidler, G. Martinez, L. H. Seeley, K. H. Kim, E. A. Behne, S. Zaranek, B. D. Chapman, S. M. Heald, and D. L. Brewe, Phys. Rev. E **62**, 8175 (2000).
[28] P. Philippe and M. Badiane, Phys. Rev. E **87**, 042206 (2013).
[29] S. E. Mena, L. Luu, P. Cuéllar, P. Philippe, and J. S. Curtis, AIChE J. **63**, 1529 (2017).
[30] J. A. Dijksman, F. Rietz, K. A. Lőrincz, M. van Hecke, and W. Losert, Rev. Sci. Instrum. **83**, 011301 (2012).
[31] J. Ngoma, P. Philippe, S. Bonelli, F. Radjai, and J. Y. Delenne, Phys. Rev. E **97**, 052902 (2018).
[32] X. Cui, J. Li, A. Chan, and D. Chapman, Particuology **10**, 242 (2012).
[33] E. P. Montellà, M. Toraldo, B. Chareyre, and L. Sibille, Phys. Rev. E **94**, 052905 (2016).
[34] X. Cui, J. Li, A. Chan, and D. Chapman, Powder Technol. **254**, 299 (2014).
[35] Y. Tang, D. H. Chan, and D. Z. Zhu, J. Eng. Mech. **143**, 04017104 (2017).
[36] P. G. Drazin and W. H. Reid, *Hydrodynamic Stability* (Cambridge University Press, Cambridge, 2004).
[37] J. Bear, *Dynamics of Fluids in Porous Media* (Dover Publications, New York, 1988).